


Article

Composition Optimum Design and Strengthening and Toughening Mechanisms of New Alumina-Forming Austenitic Heat-Resistant Steels

Nan Dong ^{1,*} , Ruirui Jia ¹, Jian Wang ¹ , Guangwei Fan ², Xudong Fang ² and Peide Han ^{1,*}¹ College of Materials Science and Engineering, Taiyuan University of Technology, Taiyuan 030024, China² Technology Center, Taiyuan Iron and Steel (Group) Co., Ltd., Taiyuan 030003, China* Correspondence: dongnantyut@126.com (N.D.); hanpeide@tyut.edu.cn (P.H.);
Tel.: +86-182-340-89854 (N.D.); +86-351-601-8843 (P.H.)

Received: 29 June 2019; Accepted: 19 August 2019; Published: 23 August 2019



Abstract: In order to promote the development of ultra-supercritical technology, the optimum composition design of three new alumina-forming austenitic heat-resistant steels, based on Fe–22Cr–25Ni (wt. %), with low cost and excellent performance, and used for 700 °C ultra-supercritical unit was carried out using Thermo-Calc software. A comparison of the mechanical properties presented that with increasing Al content, the plasticity of the system was further improved. Based on the composition system, a systematic investigation regarding the structure stability, thermodynamic properties, and mechanical properties of these new steels was carried out to reveal possible strengthening and toughening mechanisms by employing the first-principles method. Calculation results showed that when Al existed in the Fe–Cr–Ni alloy system as a solid solution, the new structures were stable, especially under high temperature. The solution of Al and Al + Si could increase the value of B/G, namely improving the plasticity of the system, particularly in case of alloying with Al + Si. The inclusion of Si in the Fe–Cr–Ni–Al system was conducive to further improving the plasticity without affecting the strength, which provided references for the subsequent optimum composition design and performance regulation of alumina-forming austenitic heat-resistant steels.

Keywords: alumina-forming austenitic heat-resistant steels; optimum design; First-principles; mechanical properties; alloy elements

1. Introduction

Environmental protection and energy conservation have been regarded as international issues in recent years. As one of the most important methods used to generate electricity, coal-fired thermal power generation often causes two key issues: environmental pollution and low thermal efficiency. Due to the increasing demands for electric power around the world, the development of clean and efficient coal-fired thermal power generation with lower fuel costs and lower emissions is being pursued in the medium- to long-term future [1]. The efficiency of electricity generation is positively related to the steam conditions (temperatures and pressures) [2]. However, increases in operating temperature and pressure present many challenges for materials with both excellent oxidation and mechanical properties. Conventional austenitic heat-resistant steels, such as HR3C, TP310HCbN, SUPER304H, and NF709, are commonly used in 600–650 °C ultra-supercritical (USC) conditions as superheater tubes and reactor pressure vessels with excellent high-temperature creep property and oxidation stability [3–7]. However, these steels face challenges in water–steam environments when the service temperature is higher than 650 °C, including the sharply deteriorated oxidation resistance caused by the formation

of volatile $\text{CrO}_2(\text{OH})_2$ species and destruction of the Cr_2O_3 -based protective scale [8–10], and poor microstructure stability [11,12], thus limiting their use at temperatures higher than 650 °C. Facing the demand for development of higher grade supercritical units, it is urgent to develop heat-resistant materials with better high-temperature oxidation resistance and creep resistance [13].

The new alumina-forming austenitic (AFA) [14–22] steels with excellent high-temperature oxidation resistance through the formation of protective Al_2O_3 and Cr_2O_3 scales and creep resistance via the dispersive precipitation of nanoscale NbC-type carbide strengthening will be the high-temperature candidate materials for the next generation of USC units [14]. Furthermore, the new AFA steels have shown promising yield and fracture stress and elongation at high temperatures, making them promising for industrial applications [16,23–26]. The key challenge for AFA steels is to maintain a single austenitic matrix phase and to form continuous protective Al_2O_3 and Cr_2O_3 scales [15]. As we know, Al and Cr can promote the formation of oxide scales; however, high contents may weaken the stability of the austenitic phases. Ni as an austenitic stabilizer can change the amount of the NiAl precipitated phases and alter the Al content in the matrix. Thus, the equilibrium concentrations of Al, Cr, and Ni are important for obtaining a single austenitic matrix and forming continuous protective Al_2O_3 and Cr_2O_3 scales [17,18,27–29].

At present, the research on AFA steels has mainly focused on the alloy system high-temperature ultrafine precipitation-strengthened (HTUPS) steels Fe–(12–15)Cr–20Ni and NF709 steels Fe–20Cr–25Ni, while less focus has been turned to AFA steels used in USC conditions higher than 650 °C. For HR3C steel (Fe–25Cr–20Ni–Nb–N), commonly used in 600–650 °C USC conditions, structural stability is poor and the precipitated phase amounts are increased under higher service temperatures [7,30]. Thus, it is urgent to develop new AFA heat-resistant steels with low cost and excellent performance, to be used for higher grade USC conditions. In this paper, three new high Cr and high Ni AFA heat-resistant steels based on the Fe–25Cr–20Ni (wt. %) were optimally designed using Thermo-Calc software. According to the compositions of the new steels, experimental steels with different amounts of Al were prepared through melting, casting, and hot rolling. After solution-treating, tensile tests were carried out to analyze their mechanical properties. In order to reveal possible strengthening and toughening mechanisms at the atomic scale of these new steels, the effects of alloy elements on their structural stabilities, thermodynamic properties, mechanical properties, and electronic properties were thoroughly investigated using the first-principles method. The results could provide suggestions for the rational design of high-performance stainless steel to be used in advanced ultra-supercritical boilers.

2. Experiment and Calculation Details

According to the compositions of the three new AFA heat-resistant steels designed using Thermo-Calc software (Thermo-Calc Software 2015b, Solna, Sweden), experimental steels with different amounts of Al were prepared in a 50 kg vacuum induction furnace (DDVIF-50-120-2.5, Dongda Advanced Material Preparation Technology Engineering Research Center, Shenyang, China) using commercially pure elements, and named 1.5Al, 2.5Al, and 3.5Al steels. After melting and casting, the ingots were hot rolled to slab with a thickness of 20 mm. The alloys were eventually solution-treated at 1260 °C for 2 h, and subsequently water-quenched to eliminate precipitation of the second phase. The chemical compositions of the three new AFA steels were analyzed using an inductively coupled plasma (ICP) spectrometer (Agilent 7500, Agilent Technology, Palo Alto, CA, USA). The mechanical tensile tests were according to the GB/T228.1-2010 standard. The size of the test samples is shown in Figure 1. Dog-bone-shaped specimens with a gauge cross section of 7 mm × 3.5 mm and a gauge length of 40 mm were cut from the solution-treated AFA steels using a wire-cut electrical discharge machine (DK7720, Huadong Automation Co., Ltd., Taizhou, China), and then the surface was polished to a mirror-like finish. The tensile tests were carried out on an Instron 5582 testing machine (Instron, Boston, MA, USA) at a strain rate of $2.5 \times 10^{-4} \text{ s}^{-1}$; the corresponding loading rate was 0.6 mm/min. Moreover, three identical specimens were measured to ensure that accurate experimental data were obtained.

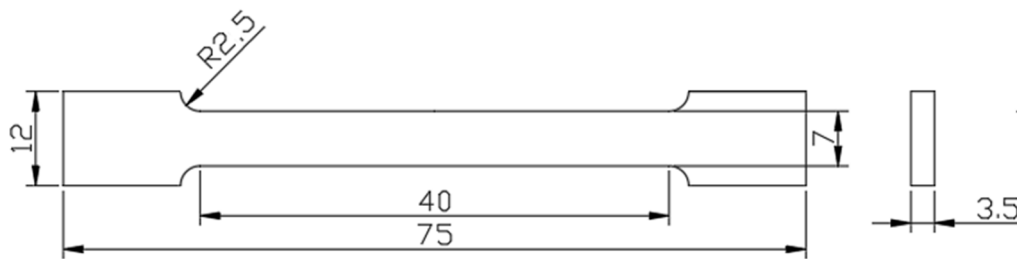


Figure 1. The size of test sample (units: mm).

First-principles calculations were performed using the Cambridge Serial Total Energy Package (CASTEP)CASTEP code based on density functional theory (DFT) [31]. The Perdew–Burke–Ernzerhof (PBE) functional within the generalized gradient approximation (GGA) was applied to describe the exchange–correlation potential [32]. The states of Fe $3d_64s_2$, Cr $3d_54s_1$, Ni $3d_84s_2$, Al $3s_23p_1$, and Si $3s_23p_2$ were treated as valence states. Interactions between the valence electrons and the ionic cores were described by the Ultrasoft pseudopotentials. A kinetic cutoff energy of 500 eV was used for plane wave expansions. Finally, a uniform k-point grid of $4 \times 4 \times 7$ for the Brillouin zone was used for all calculations [33]. In calculations, all atoms were fully relaxed until the convergence parameters satisfied the following conditions: total energy tolerance, 1.0×10^{-5} eV/atom; maximum force tolerance, 0.3 eV/nm; maximal stress component, 0.03 GPa; and maximal displacement, 1×10^{-4} nm. Using the current theoretical scheme, the calculated lattice constant (a) of the face-centered cubic (fcc) Fe solid was 3.44 Å, which was in good agreement with the previously reported values of 3.45 Å [34] and 3.43 Å [35]. The bulk modulus (B) was 348.51 GPa, the shear modulus (G) was 243.34 GPa, and the Young’s modulus (E) was 592.74 GPa, which were close to the values reported in another paper [34], which reported the bulk modulus (B) 317 GPa, the shear modulus (G) 240 GPa, and the Young’s modulus (E) 575 GPa. The good agreement in the crystal lattice constants and elastic modulus thereby validated the application of the methodology to study the structural stability and strengthening and toughening mechanisms.

3. Results and Discussion

3.1. Composition Optimum Design

Based on the Fe–22Cr–25Ni (wt. %) system, the optimum composition design of three new alumina-forming austenitic heat resistant steels by adjusting the proportion of alloy elements such as Nb, Al, Cu, and Si, which was carried out using Thermo-Calc software. The calculated chemical compositions of these new steels were Fe–22Cr–25Ni–0.45Nb–0.80Mn–2.75Cu–0.30Si–0.07C–(1.5, 2.5, 3.5)Al (wt. %). The equilibrium volume fractions of the phases, calculated as a function of the solution temperatures of the three new steels, are shown in Figure 2. Al and Si mainly played the role of solid solution strengthening, while Nb and Cu mainly formed NbX ($X = C, N$) and copper nanoscale precipitation phases [24,36,37]. At wide high-temperature ranges, only single austenite phases were observed in the three new steels, without any other precipitation phases. This was beneficial for the hot rolling process. At lower temperatures, body-centered cubic (bcc) phases, σ phases, and $M_{23}C_6$ could precipitate in the new steels, which reduced the stability of the austenite phase. Specifically, the content of Al had a significant influence on the precipitation temperature and amount; the larger the content of Al, the higher the precipitated temperature region and larger the precipitated phase amounts. Fortunately, σ phases, the hardest and most brittle, precipitated mainly at 450–700 °C. The precipitation temperatures were all outside the range of the designed operating temperature.

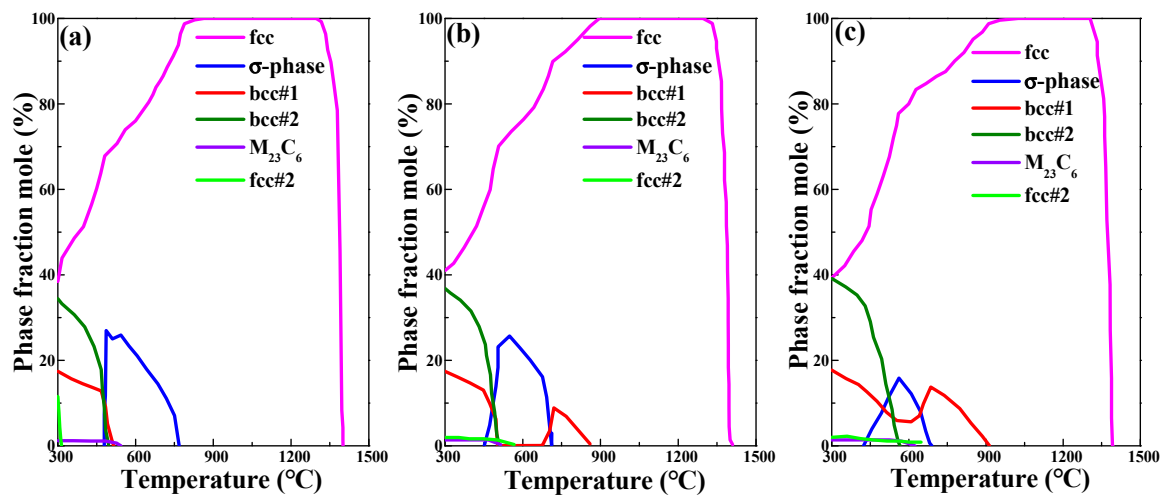


Figure 2. Equilibrium phase diagrams of new alumina-forming austenitic heat-resistant steels: (a) 1.5Al; (b) 2.5Al; (c) 3.5Al.

According to the compositions designed above, the corresponding experimental steels were prepared in a vacuum induction furnace. In order to weaken the elements' segregation and reduce the harmful influence of precipitated phases, the steels were eventually solution-treated at 1260 °C for 2 h. The microstructures of the new AFA steels after solid solution treatment are presented in Figure 3. It can be seen that all the matrices of the steels were composed of a single austenite phase. The analyzed chemical compositions of the new AFA steels, which were confirmed by an ICP spectrometer, are shown in Table 1.

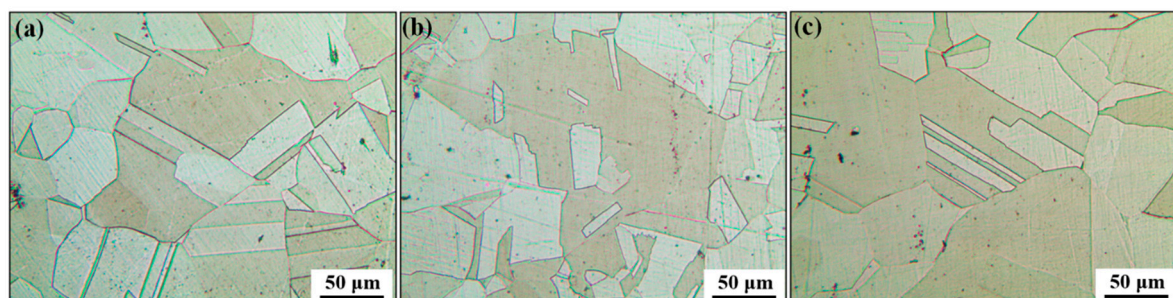


Figure 3. Equilibrium phase diagrams of new alumina-forming austenitic heat-resistant steels: (a) 1.5Al; (b) 2.5Al; (c) 3.5Al.

Table 1. Chemical compositions of the new alumina-forming austenitic heat-resistant steels (wt. %).

Alloy	Cr	Ni	Al	Nb	Mn	Cu	Si	C	Fe
1.5Al	21.19	25.12	1.50	0.44	0.80	2.60	0.30	0.07	Bal
2.5Al	21.36	24.59	2.48	0.42	0.77	2.65	0.28	0.07	Bal
3.5Al	22.14	25.29	3.51	0.40	0.78	2.63	0.29	0.07	Bal

3.2. Mechanical Properties

The stress–strain curves under room temperature are presented in Figure 4. The tensile curves of the three steels were basically similar. For 1.5Al, 2.5Al, and 3.5Al steels, the average ultimate tensile strengths were 559.6 MPa, 561.8 MPa, and 569.8 MPa, respectively. The uniform elongations were 56.6%, 57.3%, and 60.2%, respectively. On the whole, with increased Al content, the strengths and plasticities of the three steels increased slightly. The strengths of our designed steels were close to those of the heat-resistant steels used in ultra-supercritical units at 600 °C [38]. The enhanced phase was mainly composed of niobium carbide, copper nanoscale precipitation phases, and another nanoscale

precipitated phases, while other alloying elements, such as Cr, Ni, Al, and Si, mainly stabilized the austenite phases and strengthen by solid solution. There have been many studies on the precipitated phase of niobium carbide and copper nanoscale precipitation phases [19,24,36,37,39]. These precipitated phases were also relatively stable under service conditions. While the roles of alloying elements in the austenite matrix were lacking for these new AFA heat-resistant steels, the mechanism at the atomic level was particularly unclear. Therefore, it is necessary to make a pertinent study of the effects of various elements on the structure and mechanical properties of the austenite matrix, especially the action mechanism of Al.

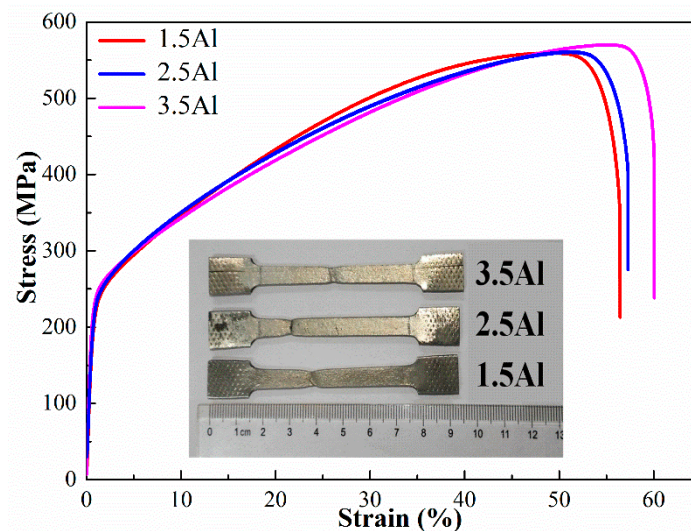


Figure 4. Stress–strain curves of new alumina-forming austenitic heat-resistant steels at room temperature.

3.3. Structure Stability and Strengthening and Toughening Mechanisms

The above experimental results indicated that the matrix austenite phases of the three new AFA heat-resistant steels were mainly composed of Cr, Ni, Al, and Si. In this section, the effects of these alloy elements on the structure stabilities, thermodynamic properties, and mechanical properties of the three new steels were thoroughly investigated to reveal possible strengthening and toughening mechanisms at the atomic scale.

3.3.1. Calculation Models

As an austenitic stainless steel, Fe crystallizes in the fcc structure. In order to keep up the fcc crystal lattice periodicity, an expanded lattice cell with 16 metallic atoms (supercell: $2 \times 2 \times 1$), $\text{Fe}_8\text{Cr}_4\text{Ni}_4$, was chosen for the calculations corresponding to the composition of Fe–22Cr–25Ni (wt. %). In the case of the new AFA heat-resistant steels, Al and Si atoms were introduced into the systems by replacing Fe atoms, corresponding to $\text{Fe}_7\text{Cr}_4\text{Ni}_4\text{Al}$, $\text{Fe}_6\text{Cr}_4\text{Ni}_4\text{Al}_2$, $\text{Fe}_5\text{Cr}_4\text{Ni}_4\text{Al}_3$, and $\text{Fe}_6\text{Cr}_4\text{Ni}_4\text{AlSi}$; all crystals belonging to the same space group (tetragonal system). The models are shown in Figure 5. The grey spheres represent Fe atoms, blue spheres are Cr atoms, pink spheres stand for Ni atoms, green spheres stand for Al atoms, and yellow spheres correspond to Si atoms. Using the equilibrium structure, the elastic constants and modulus of different systems were calculated through the stress–strain method based on a generalized Hooke's Law [40]: $\sigma_{ij} = C_{ijkl}\epsilon_{kl}$, where σ_{ij} is the tensile stress and ϵ_{kl} is the longitudinal strain. The thermodynamic properties of the considered system under high temperatures were calculated based on the frequency analysis.

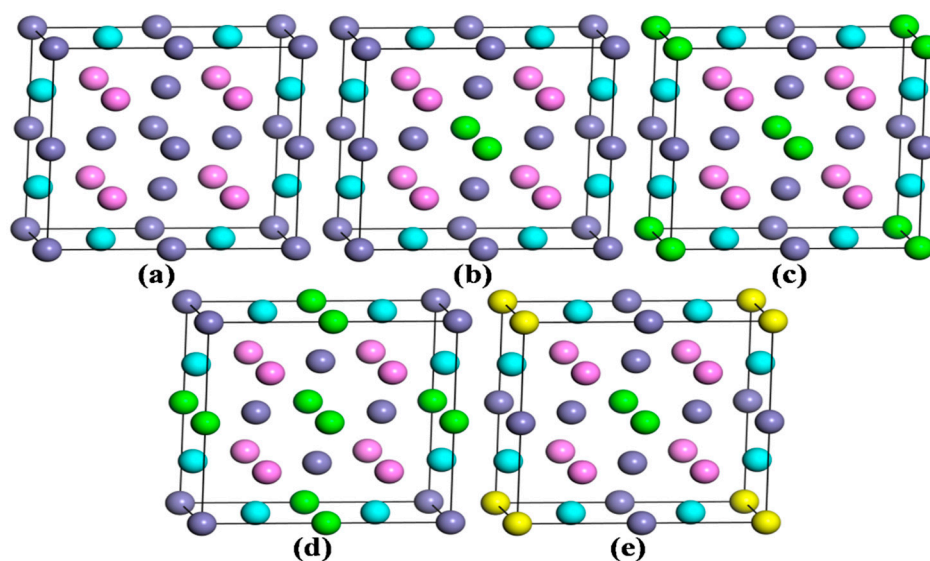


Figure 5. Schematic diagram of models for calculations: (a) $\text{Fe}_8\text{Cr}_4\text{Ni}_4$; (b) $\text{Fe}_7\text{Cr}_4\text{Ni}_4\text{Al}$; (c) $\text{Fe}_6\text{Cr}_4\text{Ni}_4\text{Al}_2$; (d) $\text{Fe}_5\text{Cr}_4\text{Ni}_4\text{Al}_3$; (e) $\text{Fe}_6\text{Cr}_4\text{Ni}_4\text{AlSi}$.

3.3.2. Structural Stability

The energetic relative stabilities of $\text{Fe}_8\text{Cr}_4\text{Ni}_4$, $\text{Fe}_7\text{Cr}_4\text{Ni}_4\text{Al}$, $\text{Fe}_6\text{Cr}_4\text{Ni}_4\text{Al}_2$, $\text{Fe}_5\text{Cr}_4\text{Ni}_4\text{Al}_3$, and $\text{Fe}_6\text{Cr}_4\text{Ni}_4\text{AlSi}$ can be discussed considering our calculations. The formation energies of different systems can be defined by Equation (1):

$$E_f = \frac{1}{\sum N_i} [E_{\text{total}} - \sum (N_i E_{\text{atom}})] \quad (1)$$

where E_{total} is the calculated total energy of the system, N_i denotes the number of atomic species i ($i = \text{Fe}, \text{Cr}, \text{Ni}, \text{Al}, \text{or Si}$) in the unit cell, and E_{atom} is the energy per atom i at their most stable state (pure constituents). The pure constituents of Fe (fcc), Cr (bcc), Ni (fcc), Al (fcc), and Si (diamond structure) were used to calculate the forming energy. When E_f is negative, it indicates that the system is easy to form, i.e., a spontaneous process, and the greater the absolute value, the easier it is to form. On the contrary, when E_f is positive, it means that the system is not easy to form, and the formation process is a process that absorbs energy. The calculated formation energies are presented in Figure 6a. It is worth noting that the formation energies were all negative, which showed that these systems were easily crystallized. As different contents of Al were introduced to the $\text{Fe}_8\text{Cr}_4\text{Ni}_4$ system, the values of $\text{Fe}_7\text{Cr}_4\text{Ni}_4\text{Al}$, $\text{Fe}_6\text{Cr}_4\text{Ni}_4\text{Al}_2$, and $\text{Fe}_5\text{Cr}_4\text{Ni}_4\text{Al}_3$ were lower than that of $\text{Fe}_8\text{Cr}_4\text{Ni}_4$, which indicated that the substitution element Al was easy to dissolve in the $\text{Fe}_8\text{Cr}_4\text{Ni}_4$ system. With an increasing number of introduced Al atoms, the formation energy became much smaller, showing that these alloys became much more easily crystallized. As Al and Si were introduced into the system simultaneously, the value of E_f was lower than for of $\text{Fe}_8\text{Cr}_4\text{Ni}_4$ and $\text{Fe}_7\text{Cr}_4\text{Ni}_4\text{Al}$, which indicated that the coordination of Si and Al was easier to dissolve in the austenite phases.

To further understand the structural stability of the different systems, we calculated their bonding energies, defined as Equation (2):

$$E_b = \frac{1}{\sum N_i} [E_{\text{total}} - \sum (N_i E_{\text{iso}}^i)] \quad (2)$$

where E_{iso}^i is the energy of isolated atom i ($i = \text{Fe}, \text{Cr}, \text{Ni}, \text{Al}, \text{or Si}$). The total energies of isolated atoms were calculated by putting a Fe, Cr, Ni, Al, or Si atom in the middle of a lattice constant of a 10 \AA cubic unit cell and taking values from the CASTEP output files directly. The term “bonding energy” refers to the energy that is released upon the creation of a bound state and which is used to

compare the relative stabilities of structural properties. A negative value of bonding energy indicates that the structure is stable. The greater the absolute value, the more stable the structure is, and the stronger the ability to resist external damage will be. To a certain extent, the bonding energy has a positive correlation with the bulk modulus. The greater the absolute value of the bonding energy, the greater the bulk modulus [41]. The calculated bonding energies are shown in Figure 6b. It was clearly seen that all bonding energies were negative, which indicated that these solid solutions were structurally stable. As different contents of Al were introduced to the $\text{Fe}_8\text{Cr}_4\text{Ni}_4$ system, the bonding energy values increased slightly, which indicated that the bonding between different atoms became weaker, finally decreasing the stability of the structure. With an increasing number of introduced Al atoms, the bonding energy values of the Fe–Cr–Ni–Al systems became larger, showing that these alloys became less stable and the interactions between atoms in the structures became much weaker. As Al and Si were introduced into the system simultaneously, the value of E_b was close to that of $\text{Fe}_7\text{Cr}_4\text{Ni}_4\text{Al}$. However, the values of E_b were all scaled between -10.0 and -8.5 eV/atom, showing that the structures were also very stable.

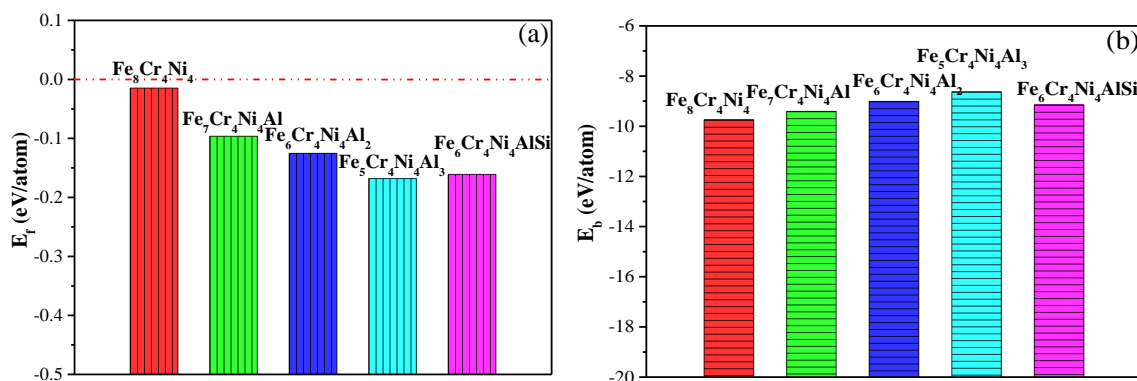


Figure 6. (a) Formation energy E_f and (b) binding energy E_b of $\text{Fe}_8\text{Cr}_4\text{Ni}_4$, $\text{Fe}_7\text{Cr}_4\text{Ni}_4\text{Al}$, $\text{Fe}_6\text{Cr}_4\text{Ni}_4\text{Al}_2$, $\text{Fe}_5\text{Cr}_4\text{Ni}_4\text{Al}_3$, and $\text{Fe}_6\text{Cr}_4\text{Ni}_4\text{AlSi}$.

3.3.3. Thermodynamic Stability

Thermodynamic properties are used to describe the structural stabilities of different systems with elevated temperatures, especially the Gibbs free energy. The calculated Gibbs free energies of different structures as a function of temperature from 0 to 1000 K are shown in Figure 7. It was found that the value of the Gibbs free energy gradually decreased, and the difference between different systems was very small. Comparing the Gibbs free energies of different structures at the same temperature, the Gibbs free energy of $\text{Fe}_8\text{Cr}_4\text{Ni}_4$ was the smallest, then $\text{Fe}_7\text{Cr}_4\text{Ni}_4\text{Al}$, $\text{Fe}_6\text{Cr}_4\text{Ni}_4\text{AlSi}$, $\text{Fe}_6\text{Cr}_4\text{Ni}_4\text{Al}_2$, and finally, $\text{Fe}_5\text{Cr}_4\text{Ni}_4\text{Al}_3$. As we know, the smaller the value of the Gibbs free energy, the better the thermal stability of the system [42,43]. A negative Gibbs free energy indicates that the structural stability exists; while a positive Gibbs free energy indicates that structural instability exists. Hence, the calculated results showed that the thermal stability of these structures gradually increased and the stable existing temperature gradually increased with elevated temperature in the order of $\text{Fe}_7\text{Cr}_4\text{Ni}_4\text{Al}$, $\text{Fe}_6\text{Cr}_4\text{Ni}_4\text{AlSi}$, $\text{Fe}_6\text{Cr}_4\text{Ni}_4\text{Al}_2$, and $\text{Fe}_5\text{Cr}_4\text{Ni}_4\text{Al}_3$. The results showed that the addition of Al and Si weakened the thermal stability of the $\text{Fe}_8\text{Cr}_4\text{Ni}_4$ system slightly. The results were in good agreement with the bonding energy analyses in Figure 6b.

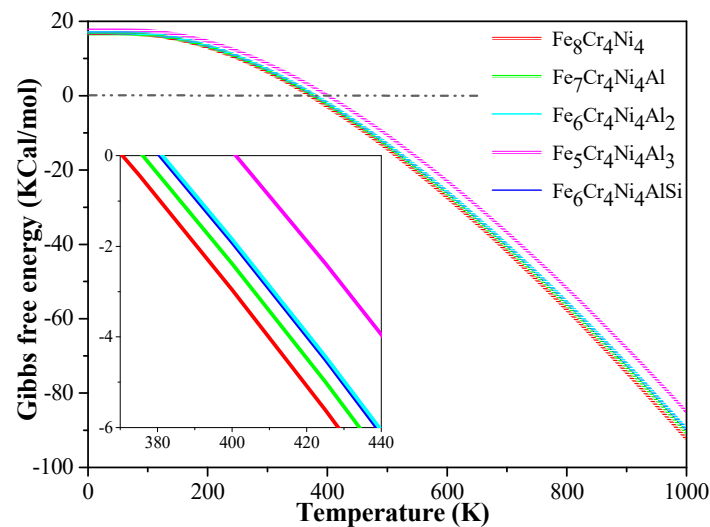


Figure 7. Relationships of Gibbs free energies with temperature of $\text{Fe}_8\text{Cr}_4\text{Ni}_4$, $\text{Fe}_7\text{Cr}_4\text{Ni}_4\text{Al}$, $\text{Fe}_6\text{Cr}_4\text{Ni}_4\text{Al}_2$, $\text{Fe}_5\text{Cr}_4\text{Ni}_4\text{Al}_3$, and $\text{Fe}_6\text{Cr}_4\text{Ni}_4\text{AlSi}$.

3.3.4. Mechanical Properties

Except for in the energy favorable condition, mechanical stability is also a necessary condition to examine the feasibility of crystal existence. The criteria of mechanical stability can be evaluated by single-crystal elastic constants according to the Born–Huang criterion, which is dependent on the crystal system. For the different crystal structures, the criteria of the mechanical stability are given as follows [44]: (i) $C_{11} > 0$, $C_{44} > 0$, $C_{11} > |C_{12}|$, and $C_{11} + 2C_{12} > 0$ for cubic crystals; (ii) $C_{11} > 0$, $C_{44} > 0$, $C_{11} > C_{12}$, and $(C_{11} + 2C_{12})C_{33} - C_{12}^2 > 0$ for hexagonal crystals; (iii) $C_{11} > 0$, $C_{22} > 0$, $C_{33} > 0$, $C_{44} > 0$, $C_{55} > 0$, $C_{66} > 0$, $C_{11} + C_{22} + C_{33} + 2(C_{12} + C_{13} + C_{23}) > 0$, $C_{11} + C_{22} - 2C_{12} > 0$, $C_{11} + C_{33} - 2C_{13} > 0$, and $C_{22} + C_{33} - 2C_{23} > 0$ for orthorhombic crystals; (iv) $C_{11} > 0$, $C_{33} > 0$, $C_{44} > 0$, $C_{66} > 0$, $C_{11} - C_{12} > 0$, $C_{11} + C_{33} - 2C_{12} > 0$, and $2(C_{11} + C_{12}) + C_{33} + 4C_{13} > 0$ for tetragonal crystals. In our calculations, all crystals were tetragonal crystals. The calculated elastic constants C_{ij} for the different structures re listed in Table 2. They showed that all calculated systems were stable according to the mechanical stability criteria. In general, all of the mechanically stable phases showed relatively higher values of C_{11} , C_{22} , and C_{33} than that of C_{44} , indicating relatively higher incompressibility along the a-, b-, and c-axes.

Table 2. Calculated single-crystal elastic constants for different systems.

Elastic Constants	C_{11}	C_{12}	C_{13}	C_{33}	C_{44}	C_{66}
$\text{Fe}_8\text{Cr}_4\text{Ni}_4$	371.484	204.667	170.828	417.936	195.492	209.082
$\text{Fe}_7\text{Cr}_4\text{Ni}_4\text{Al}$	323.440	186.422	157.412	354.115	184.691	174.932
$\text{Fe}_6\text{Cr}_4\text{Ni}_4\text{Al}_2$	271.592	169.982	149.656	298.950	170.620	147.576
$\text{Fe}_5\text{Cr}_4\text{Ni}_4\text{Al}_3$	225.141	199.483	126.016	297.716	134.792	103.835
$\text{Fe}_6\text{Cr}_4\text{Ni}_4\text{AlSi}$	298.478	211.721	178.404	364.793	168.795	133.751

Compared with single-crystal elastic properties, polycrystalline elastic properties (such as bulk modulus, shears modulus, Young’s modulus and Poisson’s ratio) usually have a higher practical application value. In order to better demonstrate the mechanical properties of polycrystalline Fe–Cr–Ni–Al(Si) systems, the bulk modulus (B) and shear modulus (G) were first calculated from the single-crystal elastic constants using the Voight–Reuss–Hill (VRH) average scheme [45].

$$B = \frac{1}{9} (C_{11} + C_{22} + C_{33}) + \frac{2}{9} (C_{12} + C_{13} + C_{23}) \quad (3)$$

$$G = \frac{1}{15} (C_{11} + C_{22} + C_{33} - C_{12} - C_{13} - C_{23}) + \frac{1}{5} (C_{44} + C_{55} + C_{66}) \quad (4)$$

The Young's modulus (E) and Poisson's ratio (ν) of these structures could then be obtained by the following equations.

$$E = \frac{9GB}{G + 3B} \quad (5)$$

$$\nu = \frac{3B - 2G}{2(G + 3B)} \quad (6)$$

With the bulk modulus and shear modulus, the macroscopic mechanical properties of different systems, such as hardness, brittleness, and toughness, could be evaluated. The Vickers hardness of different systems could be calculated by the following equation [46]:

$$H_V = 2 \left(\frac{G}{K^2} \right)^{0.585} - 3 \quad (7)$$

where $K = B/G$. According to the empirical Pugh formula, the B/G ratio is a good indicator used to distinguish a material is brittle or ductile [47], and the critical value which separates ductile and brittle materials is approximately 1.75. Ductile materials should meet $B/G > 1.75$, while values below that indicate brittleness.

Due to the anisotropy of active materials, micro-cracks could be induced in austenitic stainless steels during the practical engineering application process. To study the influence of single-crystal elastic anisotropy on their mechanical properties, we calculated the elastic anisotropy of different systems using the Zener's anisotropy parameter A_Z [46]:

$$A_Z = \frac{2C_{44}}{C_{11} - C_{12}} \quad (8)$$

All calculated mechanical properties are summarized in Figure 8a, which shows the elastic modulus of different systems. The bulk modulus B and shear modulus (G) of $Fe_8Cr_4Ni_4$ were found to be in the order of 250.40 GPa and 397.73 GPa; these values agreed to a large extent with those reported in Reference [34,48]. It was found that as different contents of Al atoms were introduced into the $Fe_8Cr_4Ni_4$ system, the bulk modulus (B), the shear modulus (G), and Young's modulus (E) all decreased slightly, demonstrating the weaker tendency of the resistant ability to deformation and the increased elasticity and compressibility in the structures. When increasing the number of introduced Al atoms, the bulk modulus (B), shear modulus (G), and Young's modulus (E) of Fe–Cr–Ni–Al systems seemed to be more sensitive to the Al content; the elastic constants became smaller, showing that the elasticity and compressibility of these alloys became much greater. As Al and Si were introduced into the system simultaneously, the bulk modulus (B), shear modulus (G), and Young's modulus (E) of the $Fe_6Cr_4Ni_4AlSi$ system became smaller, indicating that the synergistic effect of Si and Al was more pronounced.

The calculated Vickers hardness of different systems is shown in Figure 8b. $Fe_8Cr_4Ni_4$ had the highest hardness, 20.31 GPa, among these structures [49]. It could be seen that our calculated results were in good agreement with previously experimental results. As Al and Al + Si atoms were introduced into the $Fe_8Cr_4Ni_4$ systems, the hardness values became lower, showing that the strengths of these materials became weakened, and with increasing Al contents, the hardness values were much lower. The hardness results were in good agreement with the elastic constant analyses in Figure 8a.

Poisson's ratio is a measure of the expansion of a material when it is compressed in the transverse direction, and is sometimes used as an approximate measure of plastic ductility. Figure 8c shows the Poisson's ratios of different systems. As Al and Al + Si atoms were introduced into the $Fe_8Cr_4Ni_4$ systems, the Poisson's ratio generally increased, indicating an increase of plasticity and metallicity in these new structures. As the Al content increased, the Poisson's ratios of the Fe–Cr–Ni–Al systems also increased, demonstrating the greater plastic ductility.

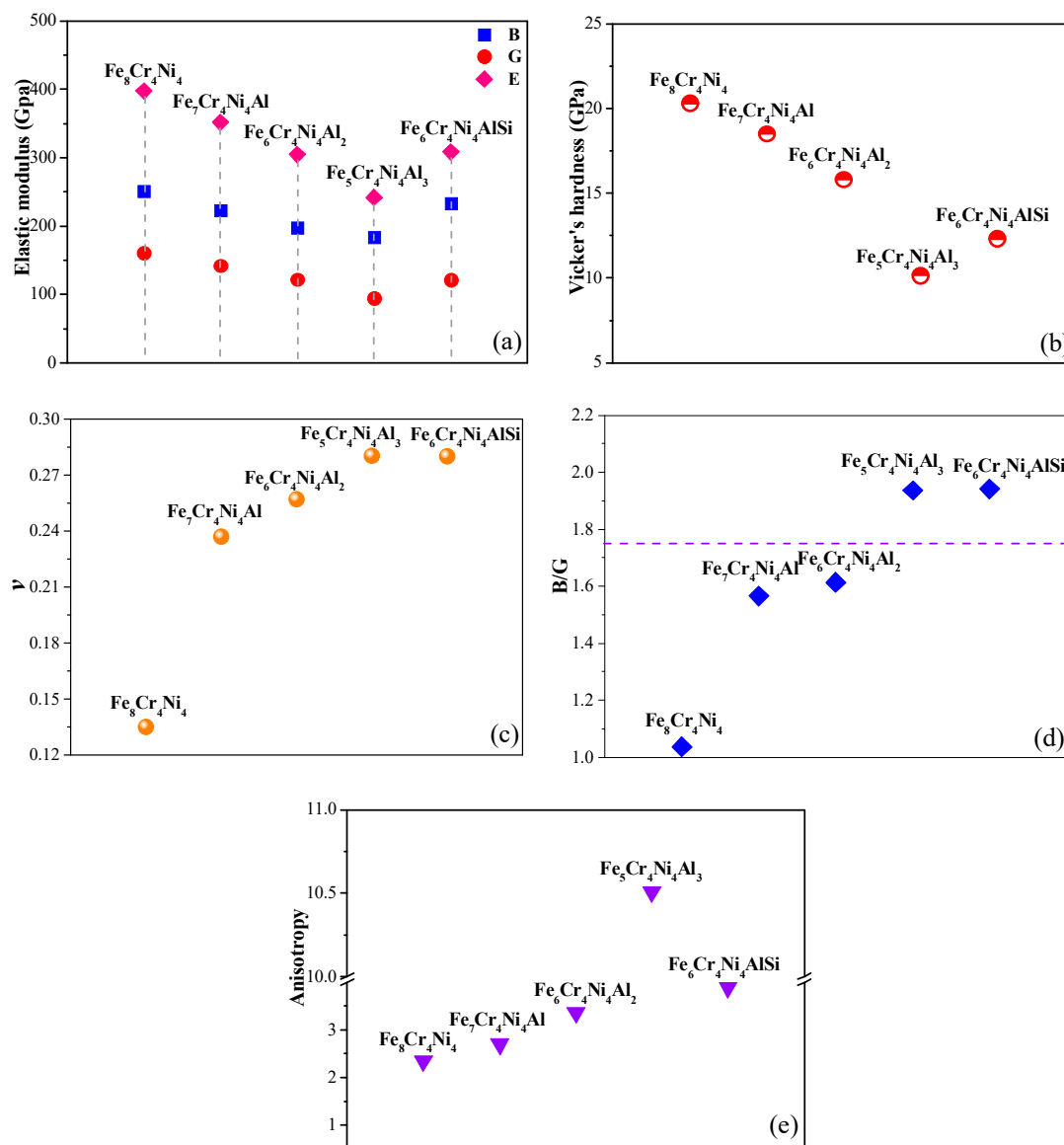


Figure 8. Calculated mechanical properties of different systems: (a) The bulk modulus (B), shear modulus (G), and Young's modulus (E); (b) the Vicker's hardness; (c) the Poisson's ratio values; (d) the B/G ratio values; (e) the Zener's anisotropy parameter A_Z .

The B/G ratio is a good indicator as to whether a material is brittle or ductile. Values above 1.75, the threshold value, indicate ductility, while values below indicate brittleness. It can be seen in Figure 8d that the values of B/G were less than 1.75 (the purple line) for Fe₈Cr₄Ni₄ system, thus, it was a brittle material. As Al and Al + Si atoms were introduced into the Fe₈Cr₄Ni₄ system, the values of B/G increased, and the calculated ratio B/G was 1.94 for Fe₆Cr₄Ni₄AlSi, corresponding to ductile behavior. Similarly, as the Al content increased, the values of B/G (1.57, 1.61, and 1.93) increased and the calculated ratio B/G was 1.93 for Fe₅Cr₄Ni₄Al₃, corresponding to ductile behavior. The results indicated that Al and Al + Si atoms could improve the plasticity and ductility of the Fe–Cr–Ni system, and the steel with Al + Si showed the most prominent effect; with increasing Al contents, the effect become more obvious. The results of B/G were in good agreement with the experimental data of elongations of the three AFA steels (56.6%, 57.3%, and 60.2%).

The degree of deviation of Zener's anisotropy parameter from unity 1 indicates the degree of elastic anisotropy. As shown in Figure 8e, a high degree of elastic anisotropy was found in Fe₈Cr₄Ni₄ with $A = 2.34$, while, as Al and Al + Si atoms were introduced into the Fe₈Cr₄Ni₄ system, the values of

A_Z became larger, indicating more anisotropy. With increasing Al contents, the values of A_Z of the Fe–Cr–Ni–Al systems also increased, and the $\text{Fe}_5\text{Cr}_4\text{Ni}_4\text{Al}_3$ had the largest value (10.51), showing the most anisotropy.

3.3.5. Electronic Properties

To further understand the nature of the structural stabilities and mechanical properties of the five different structures, the electronic properties were also analyzed. Charge density distribution can reflect the bonding characteristics between atoms. Figure 9 displays the charge density distribution maps of $\text{Fe}_8\text{Cr}_4\text{Ni}_4$, $\text{Fe}_7\text{Cr}_4\text{Ni}_4\text{Al}$, $\text{Fe}_6\text{Cr}_4\text{Ni}_4\text{Al}_2$, $\text{Fe}_5\text{Cr}_4\text{Ni}_4\text{Al}_3$, and $\text{Fe}_6\text{Cr}_4\text{Ni}_4\text{AlSi}$. For $\text{Fe}_8\text{Cr}_4\text{Ni}_4$, the valence charge densities were distributed uniformly around the Fe, Cr, and Ni atoms, and the near-spherical charge density represented the metallic bonds. As Al atoms were added into the $\text{Fe}_8\text{Cr}_4\text{Ni}_4$ system, it was seen that the area with lower electron density (the orange area) around the substitutional Al atoms became larger. With an increase of Al content, the area with lower electron density around the Al atoms became much larger, and the bonding strengths were gradually weakened. As Al and Si were introduced into the system simultaneously, the area with lower electron density around the substitutional Al and Si atoms became larger than $\text{Fe}_7\text{Cr}_4\text{Ni}_4\text{Al}$. $\text{Fe}_6\text{Cr}_4\text{Ni}_4\text{AlSi}$ showed the most obvious change. These phenomena suggested that there were significant depletions of charges around substitutional Al and Si atoms in these new systems, indicating that the bonding strengths, structural stabilities, and mechanical strengths became weakened. In summary, the charge density distribution results were accordant with those of the above structural stability and mechanical property analyses.

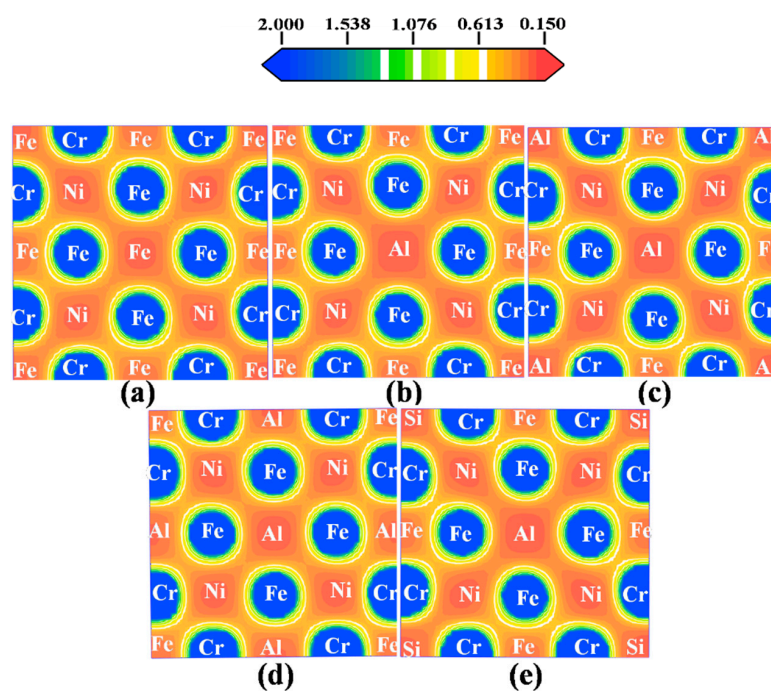


Figure 9. Charge density distribution maps of different systems in the (002) plane: (a) $\text{Fe}_8\text{Cr}_4\text{Ni}_4$; (b) $\text{Fe}_7\text{Cr}_4\text{Ni}_4\text{Al}$; (c) $\text{Fe}_6\text{Cr}_4\text{Ni}_4\text{Al}_2$; (d) $\text{Fe}_5\text{Cr}_4\text{Ni}_4\text{Al}_3$; (e) $\text{Fe}_6\text{Cr}_4\text{Ni}_4\text{AlSi}$.

We investigated the electrochemical stabilities of the different structures mentioned above by analyzing the total density of states (TDOS), as shown in Figure 10a. These structures showed very similar patterns. The finite and non-zero values of TDOS at the Fermi level indicated the metallic character of these structures. As we know, electrochemical stability is closely related to the number of electrons at the Fermi level; fewer electrons implies that higher electrochemical stability and a more stable structure. TDOS analysis suggested that the numbers of electrons at the Fermi level had significant changes with the addition of Al and Al + Si atoms. As different contents of Al were introduced to the

$\text{Fe}_8\text{Cr}_4\text{Ni}_4$ system, the numerical values decreased for $\text{Fe}_7\text{Cr}_4\text{Ni}_4\text{Al}$ (20.8 electrons/eV), $\text{Fe}_6\text{Cr}_4\text{Ni}_4\text{Al}_2$ (19.4 electrons/eV), and $\text{Fe}_5\text{Cr}_4\text{Ni}_4\text{Al}_3$ (18.1 electrons/eV), which indicated that as Al atoms were added into the $\text{Fe}_8\text{Cr}_4\text{Ni}_4$ system, the electron densities were decreased and the electrochemical stabilities were enhanced. With increasing Al contents, the numbers of electrons at the Fermi level became much smaller, and the electron densities were decreased and the electrochemical stabilities were enhanced. As Al and Si were introduced into the system simultaneously, the numerical value decreased for $\text{Fe}_6\text{Cr}_4\text{Ni}_4\text{AlSi}$ (19.4 electrons/eV), lower than that of $\text{Fe}_7\text{Cr}_4\text{Ni}_4\text{Al}$ (20.8 electrons/eV). These results indicated that as Al and Al + Si atoms were added into the $\text{Fe}_8\text{Cr}_4\text{Ni}_4$ system, the electron densities decreased and the electrochemical stabilities were enhanced.

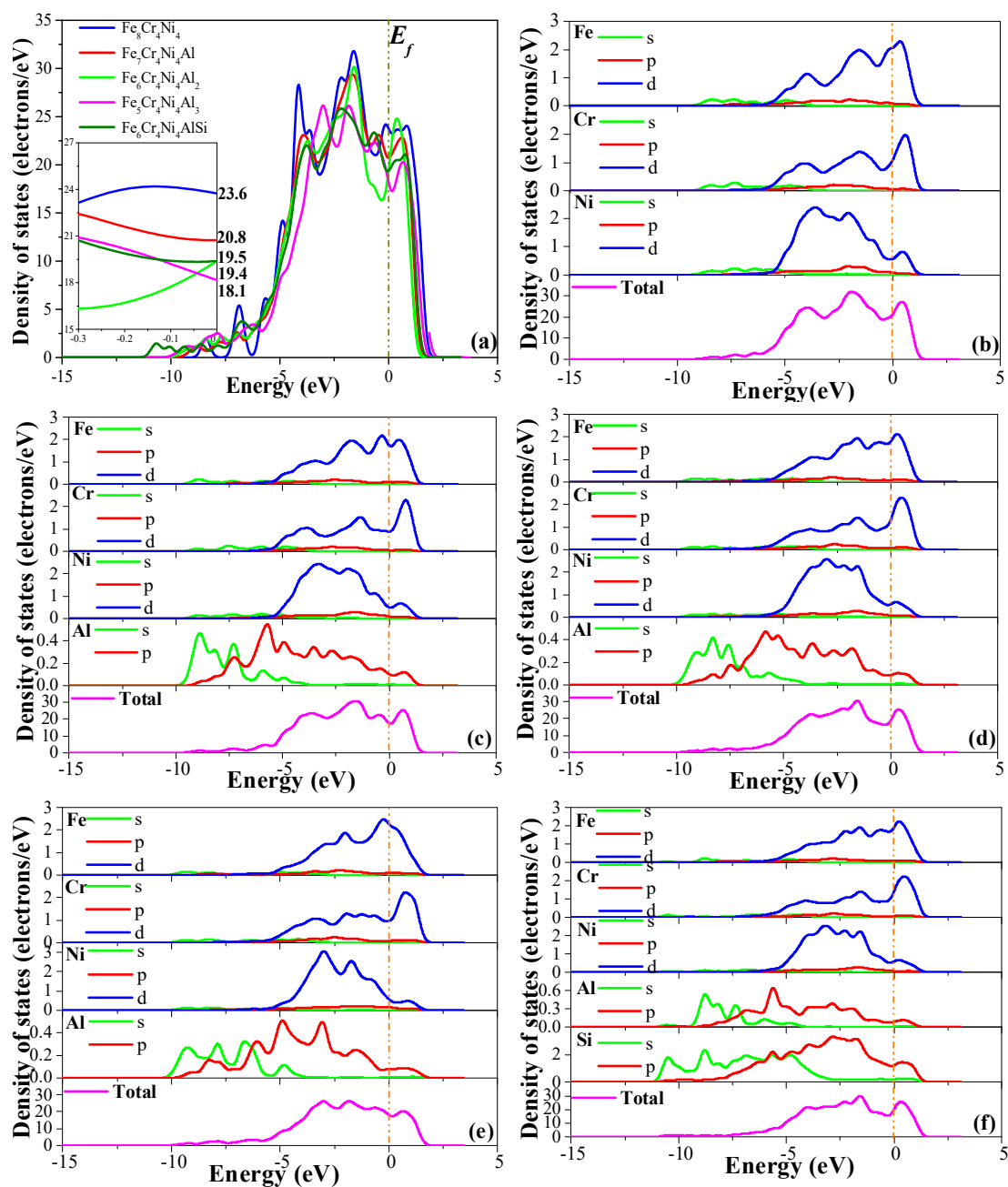


Figure 10. (a) Total density of states (TDOS) of different systems; partial density of states (PDOS) of different systems: (b) $\text{Fe}_8\text{Cr}_4\text{Ni}_4$; (c) $\text{Fe}_7\text{Cr}_4\text{Ni}_4\text{Al}$; (d) $\text{Fe}_6\text{Cr}_4\text{Ni}_4\text{Al}_2$; (e) $\text{Fe}_5\text{Cr}_4\text{Ni}_4\text{Al}_3$; and (f) $\text{Fe}_6\text{Cr}_4\text{Ni}_4\text{AlSi}$.

The partial densities of states (PDOS) of the different systems are shown in Figure 10b–f. For $\text{Fe}_8\text{Cr}_4\text{Ni}_4$, it was clearly seen that the part of TDOS below the Fermi level was mainly contributed to by Fe 3d, Cr 3d, and Ni 3d electrons, while the part of TDOS above the Fermi level was mainly occupied by Fe 3d and Cr 3d electrons. With the introduction of Al and Si atoms into the system, the Al–Fe (or Al–Cr, Al–Ni, Si–Fe, Si–Cr, Si–Ni) interactions were relatively weak because of the lack of overlap between the PDOS of Al and Fe (Cr, Ni) atoms (or Si and Fe atoms). The pseudo-gap is defined as the trough of the Fermi level, where there are two peaks of the density of state (DOS) at each side of the non-zero Fermi level. There are two mechanisms for the formation of the pseudo-gap in alloys. One is ionic origin and the other is due to hybridization effects [50–53]. The wider the splitting shape of the pseudo-gap, the stronger the hybridization effects [51,52]. As can be seen from Figure 8b, the pseudo-gap for $\text{Fe}_8\text{Cr}_4\text{Ni}_4$ was exactly at the Fermi level and was the widest among the five structures, so the hybridization effect between Fe 3d, Cr 3d, and Ni 3d electrons was the strongest, which indicated the most stable structure and the largest elastic modulus [51]. As Al and Si atoms were added into the $\text{Fe}_8\text{Cr}_4\text{Ni}_4$ system, the pseudo-gaps became smaller and the hybridization effect between Fe 3d, Cr 3d, and Ni 3d electrons became weaker. With increasing Al contents, the pseudo-gaps became much smaller and the hybridization effect between Fe 3d, Cr 3d, and Ni 3d electrons became weaker. For $\text{Fe}_5\text{Cr}_4\text{Ni}_4\text{Al}_3$ and $\text{Fe}_6\text{Cr}_4\text{Ni}_4\text{AlSi}$, the pseudo-gap had disappeared, showing that the hybridization effects between Fe 3d, Cr 3d, and Ni 3d electrons had reached the minimum and the bond interactions were the weakest, which further resulted in their lowest strength but greatest plasticity and the ductility. The results were in accordance with those of the above analyses.

4. Conclusions

On the basis of a Fe–22Cr–25Ni (wt. %) system, the optimum composition design of three new AFA heat resistant steels was carried out by adjusting the proportion of Nb, Al, Cu, and Si using Thermo-Calc software. Based on the composition system, a systematic investigation regarding the structural stability, thermodynamic properties, and mechanical properties of these new steels was carried out by employing the first-principles method to reveal possible strengthening and toughening mechanisms at the atomic scale. A comparison of the mechanical properties revealed that with increasing Al content, the plasticity of the system was further improved. The calculated formation energies, bonding energies, and Gibbs free energies indicated that Al and Al + Si were easy to dissolve in $\text{Fe}_8\text{Cr}_4\text{Ni}_4$ systems and that the structures were all stable, especially under high temperatures. A comparison of the mechanical properties showed that the solutions of Al and Al + Si could increase the value of B/G, i.e., improve the plasticity of the system, particularly in the case of alloying with Al + Si. The calculated results were in good agreement with the experimental tensile test results. The electronic structure and DOS analysis showed excellent consistency with the computation results of the energy and mechanical properties analyses. Above all, the inclusion of Si in the Fe–Cr–Ni–Al system was conducive to further improving the plasticity without affecting the strength, which can provide reference for the subsequent optimum composition design and performance regulation of AFA heat-resistant steels.

Author Contributions: Conceptualization, N.D.; methodology, N.D. and X.F.; software, N.D. and R.J.; writing—original draft preparation, N.D.; writing—review and editing, G.F. and P.H.; supervision, J.W. and P.H.; funding acquisition, N.D. and P.H.

Funding: This research was funded by the National Natural Science Foundation of China (51871159), the Natural Science Foundation of Shanxi province (201801D221125), and the Graduate Education Innovation Project of Shanxi Province (2016JD20).

Conflicts of Interest: The authors declare no conflict of interest.

References

1. Hussain, T.; Syed, A.U.; Simms, N.J. Fireside Corrosion of Superheater Materials in Coal/Biomass Co-fired Advanced Power Plants. *Oxid. Met.* **2013**, *80*, 529–540. [[CrossRef](#)]
2. Maziasz, P.J. Development of creep-resistant and oxidation-resistant austenitic stainless steels for high temperature applications. *JOM* **2018**, *70*, 66–75. [[CrossRef](#)]
3. Takahashi, T.; Sakakibara, M.; Kikuchi, M.; Ogawa, T.; Sakurai, H.; Nagao, K.; Yasuda, H. *Development of High-Strength 20Cr-25Ni (NF709) Steel for USC Boiler Tubes*; Nippon Steel Technical Report No. 38; Nippon Steel Corp: Tokyo, Japan, 1998.
4. Viswanathan, R.; Sarver, J.; Tanzosh, J. Boiler Materials for Ultra-Supercritical Coal Power Plants—Steamside Oxidation. *J. Mater. Eng. Perform.* **2006**, *15*, 255–274. [[CrossRef](#)]
5. Zhao, Y.; Zhao, J.; Li, X.N. Microstructural evolution and change in hardness during creep of NF709 austenitic stainless steel. *Acta Metall. Sin.* **2011**, *24*, 220–224.
6. Dudziak, T.; Łukaszewicz, M.; Simms, N.; Nicholls, J.R. Steam oxidation of TP347HFG, super 304H and HR3C—analysis of significance of steam flowrate and specimen surface finish. *Corros. Eng. Sci. Technol.* **2015**, *50*, 272–282. [[CrossRef](#)]
7. Vujic, S.; Sandström, R.; Sommitsch, C. Precipitation evolution and creep strength modelling of 25Cr20NiNbN austenitic steel. *Mater. High Temp.* **2015**, *32*, 607–618. [[CrossRef](#)]
8. Wright, I.G.; Dooley, R.B. A review of the oxidation behavior of structural alloys in steam. *Int. Mater. Rev.* **2010**, *55*, 129–167. [[CrossRef](#)]
9. Saunders, S.; Monteiro, M.; Rizzo, F. The oxidation behaviour of metals and alloys at high temperatures in atmospheres containing water vapour: A review. *Prog. Mater. Sci.* **2008**, *53*, 775–837. [[CrossRef](#)]
10. Jung, K.; Kim, C.S.; Pettit, F.S.; Meier, G.H. Interfacial failure via encapsulation of external particulates in an outward-growing thermal oxide. *J. Power Sources* **2011**, *196*, 4686–4694. [[CrossRef](#)]
11. Chai, G.; Boström, M.; Olaison, M.; Forsberg, U. Creep and LCF Behaviors of Newly Developed Advanced Heat Resistant Austenitic Stainless Steel for A-USC. *Procedia Eng.* **2013**, *55*, 232–239. [[CrossRef](#)]
12. Iseda, A.; Okada, H.; Semba, H.; Igarashi, M. Long term creep properties and microstructure of SUPER304H, TP347HFG and HR3C for A-USC boilers. *Energy Mater.* **2007**, *2*, 199–206. [[CrossRef](#)]
13. Liu, P.; Chu, Z.K.; Yuan, Y.; Wang, D.H.; Cui, C.Y.; Hou, G.C.; Zhou, Y.Z.; Sun, X.F. Microstructures and mechanical properties of a newly developed austenitic heat resistant steel. *Acta Metall. Sin.* **2019**, *32*, 517–525. [[CrossRef](#)]
14. Yamamoto, Y.; Brady, M.P.; Lu, Z.P.; Maziasz, P.J.; Liu, C.T.; Pint, B.A.; More, K.L.; Meyer, H.M.; Payzant, E.A. Creep-resistant, Al₂O₃-forming austenitic stainless steels. *Science* **2007**, *316*, 433–436. [[CrossRef](#)] [[PubMed](#)]
15. Brady, M.; Yamamoto, Y.; Santella, M.; Pint, B.; Brady, M.; Pint, B. Effects of minor alloy additions and oxidation temperature on protective alumina scale formation in creep-resistant austenitic stainless steels. *Scr. Mater.* **2007**, *57*, 1117–1120. [[CrossRef](#)]
16. Xu, X.Q.; Zhang, X.F.; Chen, G.L.; Lu, Z.P. Improvement of high-temperature oxidation resistance and strength in alumina-forming austenitic stainless steels. *Mater. Lett.* **2011**, *65*, 3285–3288. [[CrossRef](#)]
17. Brady, M.; Magee, J.; Yamamoto, Y.; Helmick, D.; Wang, L. Co-optimization of wrought alumina-forming austenitic stainless steel composition ranges for high-temperature creep and oxidation/corrosion resistance. *Mater. Sci. Eng. A* **2014**, *590*, 101–115. [[CrossRef](#)]
18. Yanar, N.M.; Lutz, B.S.; Garcia-Fresnillo, L.; Brady, M.P.; Meier, G.H.; Brady, M. The Effects of Water Vapor on the Oxidation Behavior of Alumina Forming Austenitic Stainless Steels. *Oxid. Met.* **2015**, *84*, 541–565. [[CrossRef](#)]
19. Zhou, D.; Zhao, W.; Mao, H.; Hu, Y.; Xu, X.; Sun, X.; Lu, Z.; Mao, H. Precipitate characteristics and their effects on the high-temperature creep resistance of alumina-forming austenitic stainless steels. *Mater. Sci. Eng. A* **2015**, *622*, 91–100. [[CrossRef](#)]
20. Gao, Q.; Qu, F.; Zhang, H.; Huo, Q. Austenite grain growth in alumina-forming austenitic steel. *J. Mater. Res.* **2016**, *31*, 1732–1740. [[CrossRef](#)]
21. Yu, Z.D.; Chen, M.H.; Shen, C.B.; Zhu, S.L.; Wang, F.H. Oxidation of an austenitic stainless steel with or without alloyed aluminum in O₂+10% H₂O environment at 800 °C. *Corro. Sci.* **2017**, *121*, 105–115. [[CrossRef](#)]
22. Baker, I.; Afonina, N.; Wang, Z.; Wu, M. Preliminary creep testing of the alumina-forming austenitic stainless steel Fe-20Cr-30Ni-2Nb-5Al. *Mater. Sci. Eng. A* **2018**, *718*, 492–498. [[CrossRef](#)]

23. Brady, M.P.; Yamamoto, Y.; Santella, M.L.; Maziasz, P.J.; Pint, B.A.; Liu, C.T.; Lu, Z.P.; Bei, H.; Brady, M.; Maziasz, P. The development of alumina-forming austenitic stainless steels for high-temperature structural use. *JOM* **2008**, *60*, 12–18. [[CrossRef](#)]
24. Bei, H.; Yamamoto, Y.; Brady, M.; Santella, M.; Brady, M. Aging effects on the mechanical properties of alumina-forming austenitic stainless steels. *Mater. Sci. Eng. A* **2010**, *527*, 2079–2086. [[CrossRef](#)]
25. Wang, M.; Sun, H.Y.; Phaniraj, M.P.; Han, H.N.; Jang, J.S.; Zhou, Z.J. Evolution of microstructure and tensile properties of Fe-18Ni-12Cr based AFA steel during aging at 700 °C. *Mater. Sci. Eng. A* **2016**, *672*, 23–31. [[CrossRef](#)]
26. Hu, B.; Baker, I. The effect of thermo-mechanical treatment on the high temperature tensile behavior of an alumina-forming austenitic steel. *Mater. Sci. Eng. A* **2016**, *651*, 795–804. [[CrossRef](#)]
27. Peraldi, R.; Pint, B.A. Effect of Cr and Ni Contents on the Oxidation Behavior of Ferritic and Austenitic Model Alloys in Air with Water Vapor. *Oxid. Met.* **2004**, *61*, 463–483. [[CrossRef](#)]
28. Sun, Y.F.; Lv, Y.Z.; Zhang, Y.; Zhao, J.Y.; Wu, Y. Microstructural and properties evolution of austenitic heat resistant steel after addition of aluminium. *Mater. Sci. Technol.* **2013**, *29*, 511–516. [[CrossRef](#)]
29. Guo, X.; Chen, K.; Gao, W.; Shen, Z.; Zhang, L. Corrosion behavior of alumina-forming and oxide dispersion strengthened austenitic 316 stainless steel in supercritical water. *Corros. Sci.* **2018**, *138*, 297–306. [[CrossRef](#)]
30. Wang, B.; Liu, Z.D.; Cheng, S.C.; Liu, C.M.; Wang, J.Z.; Liu, Z.C. Microstructure Evolution and Mechanical Properties of HR3C Steel during Long-term Aging at High Temperature. *J. Iron Steel Res. Int.* **2014**, *21*, 765–773. [[CrossRef](#)]
31. Segall, M.D.; Lindan, P.J.D.; Probert, M.J.; Pickard, C.J.; Hasnip, P.; Clark, S.J.; Payne, M.C. First-principles simulation: Ideas, illustrations and the CASTEP code. *J. Phys. Condens. Matter* **2002**, *14*, 2717–2744. [[CrossRef](#)]
32. Perdew, J.P.; Burke, K.; Ernzerhof, M. Generalized Gradient Approximation Made Simple. *Phys. Rev. Lett.* **1996**, *77*, 3865–3868. [[CrossRef](#)] [[PubMed](#)]
33. Monkhorst, H.J.; Pack, J.D. Special points for Brillouin-zone integrations. *Phys. Rev. B* **1976**, *13*, 5188–5192. [[CrossRef](#)]
34. Guo, G.Y.; Wang, H.H. Gradient-corrected density functional calculation of elastic constants of Fe, Co and Ni in bcc, fcc and hcp structures. *Chin. J. Phys.* **2000**, *38*, 949–961.
35. Haglund, J.; Guillermet, A.F.; Grimvall, G.; Körling, M. Theory of bonding in transition-metal carbides and nitrides. *Phys. Rev. B* **1993**, *48*, 11685–11691. [[CrossRef](#)] [[PubMed](#)]
36. Zhao, B.; Chang, K.; Fan, J.; Chen, Z.; Dong, X.; Zhang, L. Annealing effects on precipitation and high-temperature properties of a Cu-containing alumina-forming austenitic steel. *Mater. Lett.* **2016**, *176*, 83–86. [[CrossRef](#)]
37. Zhao, B.; Fan, J.; Chen, Z.; Dong, X.; Sun, F.; Zhang, L. Evolution of precipitates in a Cu-containing alumina-forming austenitic steel after short-term mechanical tests. *Mater. Charact.* **2017**, *125*, 37–45. [[CrossRef](#)]
38. Chi, C.Y.; Yu, H.Y.; Xie, X.S. Research and development of austenitic heat-resistant steels for 600 °C superheat/reheater tubes of USC power plant boilers. *World Iron Steel* **2012**, *4*, 50–65.
39. Moon, J.; Lee, T.H.; Heo, Y.U.; Han, Y.S.; Kang, J.Y.; Ha, H.Y.; Suh, D.W. Precipitation sequence and its effect on age hardening of alumina-forming austenitic stainless steel. *Mater. Sci. Eng. A* **2015**, *645*, 72–81. [[CrossRef](#)]
40. Fast, L.; Wills, J.M.; Johansson, B.; Eriksson, O. Elastic constants of hexagonal transition metals: Theory. *Phys. Rev. B* **1995**, *51*, 17431–17438. [[CrossRef](#)]
41. Meradji, H.; Drablia, S.; Ghemid, S.; Belkhir, H.; Bouhafs, B.; Tadjer, A. First-principles elastic constants and electronic structure of BP, BAs, and BSb. *Phys. Status Solidi (b)* **2004**, *241*, 2881–2885. [[CrossRef](#)]
42. Zhou, D.; Liu, J.; Xu, S.; Peng, P. Thermal stability and elastic properties of Mg₃Sb₂ and Mg₃Bi₂ phases from first-principles calculations. *Phys. B Condens. Matter* **2010**, *405*, 2863–2868. [[CrossRef](#)]
43. Huang, Z.W.; Zhao, Y.H.; Hou, H.; Han, P.D. Electronic structural, elastic properties and thermodynamics of Mg₁₇Al₁₂, Mg₂Si and Al₂Y phases from first-principles calculations. *Phys. B* **2002**, *407*, 1075–1081. [[CrossRef](#)]
44. Du, J.; Wen, B.; Melnik, R.; Kawazoe, Y. Phase stability, elastic and electronic properties of Cu–Zr binary system intermetallic compounds: A first-principles study. *J. Alloy. Compd.* **2014**, *588*, 96–102. [[CrossRef](#)]
45. Wu, Z.J.; Zhao, E.J.; Xiang, H.P.; Hao, X.F.; Liu, X.J.; Meng, J. Crystal structures and elastic properties of superhard IrN₂ and IrN₃ from first principles. *Phys. Rev. B* **2007**, *76*, 1–15. [[CrossRef](#)]

46. Zhu, Y.; Yan, M.; Zhang, Y.; Zhang, C. First-principles investigation of structural, mechanical and electronic properties for Cu–Ti intermetallics. *Comput. Mater. Sci.* **2016**, *123*, 70–78. [[CrossRef](#)]
47. Pugh, S. XCII. Relations between the elastic moduli and the plastic properties of polycrystalline pure metals. *Lond. Edinb. Dublin Philos. Mag. J. Sci.* **1954**, *45*, 823–843. [[CrossRef](#)]
48. Benyelloul, K.; Aourag, H. Elastic constants of austenitic stainless steel: Investigation by the first-principles calculations and the artificial neural network approach. *Comput. Mater. Sci.* **2013**, *67*, 353–358. [[CrossRef](#)]
49. Fang, Y.; Zhao, J.; Li, X. Precipitates in hr3c steel aged at high temperature. *Acta Met. Sin.* **2010**, *46*, 844–849. [[CrossRef](#)]
50. Li, K.; Xie, H.; Liu, J.; Ma, Z.; Zhou, Y.; Xue, D. From chemistry to mechanics: Bulk modulus evolution of Li–Si and Li–Sn alloys via the metallic electronegativity scale. *Phys. Chem. Chem. Phys.* **2013**, *15*, 17658–17663. [[CrossRef](#)] [[PubMed](#)]
51. Zhang, P.; Ma, Z.; Wang, Y.; Zou, Y.; Lei, W.; Pan, Y.; Lu, C. A first principles study of the mechanical properties of Li–Sn alloys. *RSC Adv.* **2015**, *5*, 36022–36029. [[CrossRef](#)]
52. Yu, R.; Chong, X.; Jiang, Y.; Zhou, R.; Yuan, W.; Feng, J. The stability, electronic structure, elastic and metallic properties of manganese nitrides. *RSC Adv.* **2015**, *5*, 1620–1627. [[CrossRef](#)]
53. Zhang, B.; Wu, L.; Wan, B.; Zhang, J.; Li, Z.; Gou, H. Structural evolution, mechanical properties, and electronic structure of Al–Mg–Si compounds from first principles. *J. Mater. Sci.* **2015**, *50*, 6498–6509. [[CrossRef](#)]



© 2019 by the authors. Licensee MDPI, Basel, Switzerland. This article is an open access article distributed under the terms and conditions of the Creative Commons Attribution (CC BY) license (<http://creativecommons.org/licenses/by/4.0/>).